Journal of the Australian Ceramic Society (2024) 60:455–469
https://doi.org/10.1007/s41779-023-00970-z

RESEARCH

Effect of replacing B_2O_3 with Dy_2O_3 on the structural, physical, and radiation shielding properties of sodium boroaluminate glass

A. A. Bendary[1] · Hosam M. Gomaa[2] · A. M. Moneep[1] · M. R. Atta[3,4] · A. S. Abdel-Moety[1] · Ali. M. Ibrahim[5,6] · M. I. Sayyed[7,8]

Received: 11 April 2023 / Revised: 28 September 2023 / Accepted: 5 November 2023 / Published online: 28 November 2023

Abstract

In this work, some transparent aluminum sodium borate-based glasses containing Dy_2O_3 have been prepared using the melt quenching method. The incorporation of Dy^{3+} ions in the glass network leads to increase and decrease the density and molar volume, respectively. The structural properties are investigated by XRD and FTIR spectroscopy. It is revealed that addition of Dy_2O_3 causes a conversion of boron coordination from BO_4 to BO_3, which indicates the increase in the number of non-bridging oxygen. Therefore, the optical band gap is found to decrease as the Dy^{3+} ions content increases. The temperature dependences of dielectric constant and AC conductivity are studied at different frequencies. The electric conductivity and dielectric parameters decrease with increasing Dy^{3+} content due to the decrease in Na^+ ions mobility due to the blocking effect of Dy^{3+} cations in the glass network. The shielding factors have been evaluated for the prepared glasses with the help of Phy-X program. The maximum linear attenuation coefficient (LAC) is found at 0.284 MeV and varied between 0.125 and 0.140 cm^{-1}. The results revealed that the incorporation of Dy_2O_3 into the glasses has a substantial effect on the $Z_{eff.}$. The value of the Z_{eff} for the D1 sample, which does not include any Dy_2O_3, stays relatively the same, ranging around 7.51. We found that the rate of reduction in Z_{eff} was significantly high when the energy of the photons is smaller than 0.826 MeV. From the Z_{eff} data, we found that the addition of Dy_2O_3 to the glasses improves both their capacity to absorb and their capability to scatter ionizing radiation.

Keywords Borate glasses · Dy_2O_3 · Optical properties · Electrical properties

✉ A. A. Bendary
dr_ayman_bendary@azhar.edu.eg

1 Physics Department, Faculty of Science, Al-Azhar University, Nasr City, Cairo 11884, Egypt

2 Pharaohs-Higher Institute for Computer, Information Systems and Management, Giza, Egypt

3 Physics Department, Faculty of Science, Al-Azhar University, Women Branch, Nasr City, Cairo 11884, Egypt

4 Present address: Physics Department, College of Science, Jouf University, Sakaka, Saudi Arabia

5 Physics Department, Faculty of Science, Aswan University, Aswan 81528, Egypt

6 Research Centre for Nano-Material Studies and their Promising Technologies, Aswan University, Aswan, Egypt

7 Department of Physics, Faculty of Science, Isra University, Amman, Jordan

8 Renewable Energy and Environmental Technology Center, University of Tabuk, Tabuk 47913, Saudi Arabia., Tabuk 47913, Saudi Arabia

Introduction

In general, glass materials have different applications. Nowadays, glasses doped with rare earth (RE^{3+}) cations are gaining more importance due to their possible integration in a wide range of potential applications, particularly in developing diverse optical and optoelectronic devices (e.g., light converters, sensors, smart windows, optical amplifier solid-state lasers, solid-state lightings (LEDs)). They are also considered good luminescence materials due to their radiation efficiencies brought by the electronic transitions between the 4f–4f and 4f–5d levels [1].

The appearance of sharp fluorescence from IR to UV regions is reasoned to the outer 5s and 5p orbitals shielding force on 4f electrons [2, 3]. Earlier studies on the optical properties of (RE^{3+}) addition on oxide glasses also showed that the emission spectra are affected by the host matrix and may be readily modified by the properties selection of the network formers and modifiers glasses [4–9]. The high

absorption of borate glasses doped rare earth ions in the UV region makes them beneficial for the UV blocking, detection of X-ray radiation, and high energy physics [10].

The borate glasses as widely used hosts offer high transparency, coordination geometry, high bond strength, low melting point, and most importantly large (RE^{3+}) ion solubility [9]. Furthermore, these glasses provide interesting optical and structural properties [11, 12]. In silicate and borate glasses, the increasing additions of Dy_2O_3 that replace either silicate or borate in the glass caused increasing values of density. Furthermore, the refractive index of the produced glass also increased [13].

The increase in refractive index with increasing the addition of Dy_2O_3 depends on the formation of bridging and non-bridging oxygen atoms [13]. Accordingly, several efforts have been dedicated to studying the structure and physical properties of such glasses, where it was found that the low-temperature conductivity is increased with the existence of Al^{3+} [14] and the addition of Al_2O_3 into the glass networks increases their stability and ionic conductivity [14]. Likewise, borate glasses doped with Dy_2O_3 are essential for potential applications such as solid-state lighting, broadband amplifiers, laser hosts, luminescence applications, optical data storage devices, and optical fiber systems [15]. The initial addition of modifiers facilitates the transformation of BO_3 into BO_4 and subsequently leads to non-bridging oxygen (NBO) formation [16]. The current study aims to estimate the impact of Dy_2O_3 on the different properties of aluminum sodium borate glass.

Experimental

Aluminum sodium borate-based glass samples doped Dy_2O_3 with the molecular composition (70-x) B_2O_3 - 25 Na_2O - 5 Al_2O_3 - (x) Dy_2O_3 (x = 0, 0.5, 1, 1.5, and 2 mol%) were prepared via the melt quenching technique using H_3BO_3, Na_2CO_3, Al_2O_3, and Dy_2O_3 as starting raw materials with purity greater than 99 %. The batches were melted in porcelain crucibles in an electric furnace for 2 h at 1100 °C. The melts were stirred several times during the melting process to ensure complete homogeneity and eventually poured between two pre-cooled stainless-steel plates kept in atmospheric conditions.

Table 1 lists the chemical compositions and sample codes of the obtained solid glasses. Density measurements were performed by applying the Archimedes method using CCl_4 as immersion liquid at room temperature. An electric balance with a sensitivity of 10^{-4} g was used to obtain samples weights in both air and liquid. FTIR spectra were collected in the range 400–4000 cm^{-1} using Varian 660-FTIR Spectrophotometer. The optical transmittance (T) and the reflectance (R) spectra were recorded at room temperature in the range 200–2500 nm using a double beam spectrometer (model, SHIMADZU UV-2100) with an accuracy of ±1 nm and ±0.3% for λ and T, respectively. For electrical measurements, each sample was polished at both sides to obtain a suitable disk, and two faces were then coated with air-drying silver paste acting as metallic electrodes. The data were collected using Stanford LCR bridge model SR 720 at four different frequencies (120, 10^3, 10^4, and 10^5 Hz), and all measurements were performed in the temperature range 300–675 K.

Result and discussion

Structural identification

The estimated glasses have been prepared and characterized using Fourier transform infrared spectra (FTIR), bulk density measurements, and molar volume calculations. Fig. 1

Table 1 The chemical compositions and sample codes

Sample	*Composition*			
	B_2O_3	Al_2O_3	Na_2O	Dy_2O_3
Dy_0	70	5	25	0
Dy_1	69.5			0.5
Dy_2	69			1
Dy_3	68.5			1.5
Dy_4	68			2

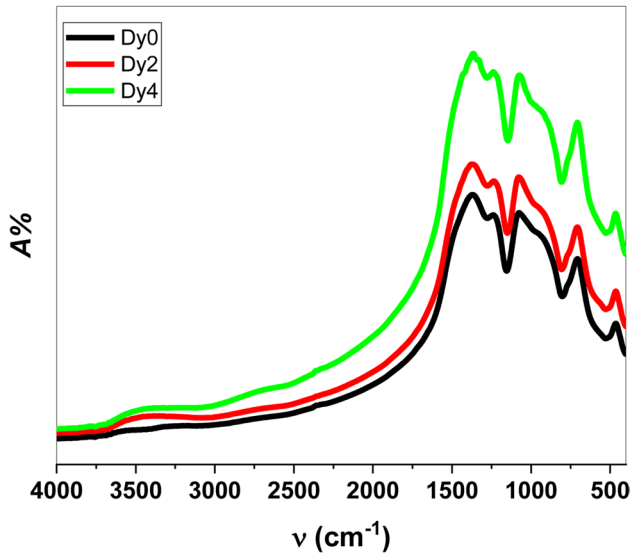

Fig. 1 The obtained FTIR spectra for the samples Dy0, Dy2, and Dy4

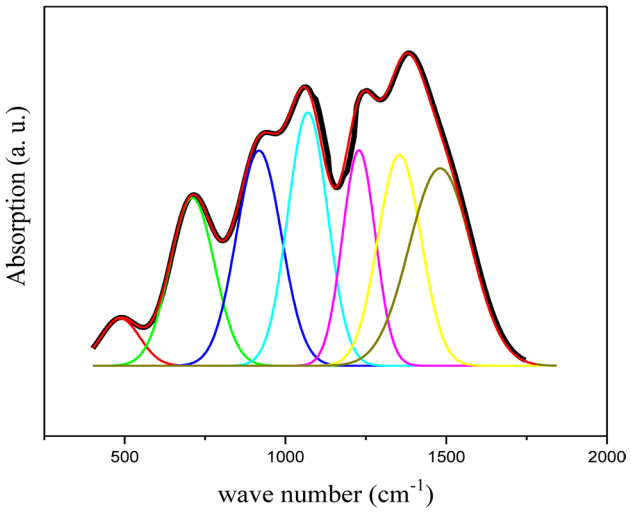

Fig. 2 The deconvoluted process applied to the IR spectrum of sample Dy_0

displays the FTIR spectra of the prepared samples over the wavenumber range from 400 to 4000 cm^{-1}. As shown, the FTIR chart of each sample is composed of a set of overlapping broad bands, which reveals the amorphous nature of the obtained solids. The similarity, as well as symmetry between the FTIR spectra, indicates that the glass network is not significantly affected by the additives of Dy_2O_3 at the expense of B_2O_3. It is well known that the FTIR spectral analysis is a significant technique that helps in recognizing the building units in the glass network. On the other side, the vibrational process of glass samples is fundamentally active in the region of 400–1700 cm^{-1}, so the measured FTIR spectra have deconvoluted, using computerized software based on the Gaussian distribution function, just over the region of 400–1700 cm^{-1}, as shown in Fig. 2 for Dy-free sample (Dy_0) as a representative sample because all samples exhibit practically similar behavior. The deconvolution process resulted in a set of vibrational peaks that were assigned to their sources based on some previously published similar studies. The band positioned at ~450–470 cm^{-1} may be due to the B–O–O bending vibration as well as the specific vibration of Na^+ cations [17, 18]. The narrow bands that located at about 536 cm^{-1} may be due bending vibrations of Dy–O linkages [7, 9, 19, 20]. The band at 570–600 cm^{-1} may be due to B–O–B stretching vibration related to oxygen atoms out ring borate [9, 21]. The peak centered at ~690–710 cm^{-1} can be assigned to an overlapping between B–O–B bending vibration of BO_3 groups and the Al–O bending vibration of in AlO_4 tetrahedral [5, 21–23]. At ~950 cm^{-1} vibrations of pentaborate groups with BO_4 tetrahedral was observed [9, 18]. The band near 1050–1090 cm^{-1} may be corresponding to B–O stretching vibration in BO_4 units [21–26], while the peak at ~1200–1250 cm^{-1} belongs to B–O stretching bond vibrations in B_3O_6 rings [17, 26]. The band near 1330 cm^{-1} can be attributed to B–O stretching vibration in BO_3 units [24, 26]. Finally, the band located at ~1420 and 1490 cm^{-1} may be due to B–O stretching vibration in BO units as metaborate, pyroborate, and orthoborate groups [17, 21]. The absorption bands appeared in the wavenumber range from 800 to 1200 cm^{-1} are associated to the tetrahedral borate units. However, the bands situated in the wavenumber range of 1200–1600 cm^{-1} are assigned to the trigonal borate units. The relative population of the tetrahedral borate units can be estimated by

$$N_4 = \frac{A_{BO_4}}{A_{BO_4} + A_{BO_3}} \quad (1)$$

A_{BO4} and A_{BO3} are the sum of the relative areas of the bands associated to the BO_4 and BO_3 structural units, respectively. The calculated N_4 was plotted versus Dy_2O_3 content as shown in Fig. 3, which shows step decrease in the value of N_4 with the increase in Dy_2O_3 content indicating the transformation of BO_4 to BO_3 structural units. Such structural change in the borate glass network with introducing rare earth ions has been reported earlier [27]. The reduction of the N_4 indicates the increase in the number of non-bridge oxygen in the glass network [19, 28]. In other words, when the glass former oxide, B_2O_3, content decreased, and more non-bridging oxygen atoms were present, increasing the concentration of BO_3 at the expense of BO_4, increasing the free-charge carriers, which in turn increased the disorder of the structure (glass homogeneity).

The densities (ρ) of the studied samples was calculated using Eq. 2, where M_a & M_l are the mass of the glass sample

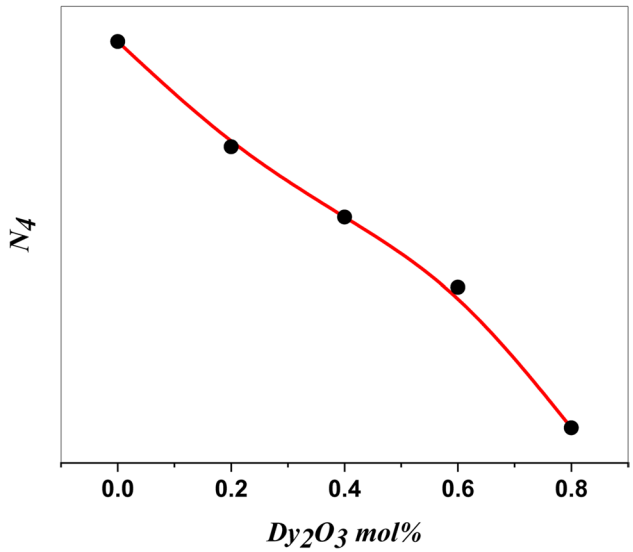

Fig. 3 N_4 value versus Dy_2O_3 content

in air and CCl_4, respectively, and ρ_l is the density of CCl_4 (ρ_l =1.587 g/cm^3), while their molar volume (V_m) values were calculated using Eq. 3, where M_i is the mean molecular weight of the glass composition.

$$\rho = \left[\frac{M_a}{M_a - M_l}\right]\rho_l \tag{2}$$

$$V_m = \left(\frac{M_i}{\rho}\right) \tag{3}$$

The obtained density and molar volume values are all listed in Table 2. It is appeared that the density increases from 2.33 to 2.62 g/cm^3 as the Dy_2O_3 content gradually increases. This can be attributed to the large molecular weight of Dy_2O_3 (372.99 g/mol) compared to B_2O_3 (69.62 g/mol). In addition, this density increase may come from the changes in the geometrical configuration and coordination of the glass network [29]. In contrast, the molar volume exhibits a slight gradual decrease with increasing Dy_2O_3 content in the glass network, thereby following the measured density inverse behavior. Based on the density measurements, the oxygen packing density (OPD) can be calculated using Eq. 4, where O is the number of oxygen atoms in the glass composition. Oxygen packing density is a measure of tightening of packing of oxide network [30].

$$OPD = \frac{\rho.\ O}{M_i} \tag{4}$$

The calculated values of OPD are inserted in Table 2. It is observed that the OPD of the investigated glasses increases with increasing Dy_2O_3 concentration indicating the enhancement of the packing tightness of the glass network.

Optical characterization

It is well known that the optical characterizations of a material in the UV-Vis spectral range are very useful to probe the fundamental absorption edge and to make the distinction between direct and indirect band gap transitions. Such optical characterizations offer a wealth of information about the structural changes of the ions that are bound in the glass network [31]. Therefore, the transmission (T) and reflection (R) spectra as a function of the wavelength (in the range 190–2500 nm) have been measured and they are presented in Fig. 4. The absorption coefficient (α) and extinction coefficient (k) of the studied glass samples can be calculated using Eqs. 5 and 6 [31], where d is the thickness of the sample.

$$\alpha = \frac{1}{d}\ln\left(\frac{1-R}{T}\right) \tag{5}$$

Table 2 Density, molar volume, and OPD of the studied samples

Sample	*ρ (g/cm^3)*	*V_m (cm/mol)*	*OPD (g. atom/l)*
Dy_0	2.33	29.77	92.37
Dy_1	2.42	29.29	93.89
Dy_2	2.50	28.93	95.06
Dy_3	2.57	28.80	95.49
Dy_4	2.62	28.74	95.69

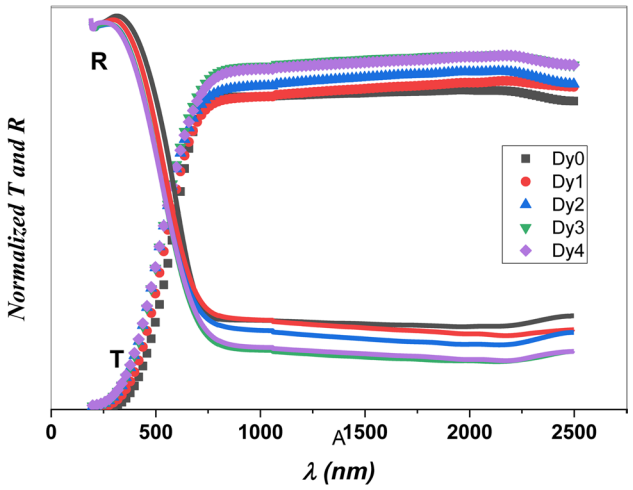

Fig. 4 Normalized transmittance and reflectance spectra of all glass samples

$$\alpha = \frac{4\pi}{k} \tag{6}$$

$$R = \frac{(1-n)^2 + k^2}{(1+n)^2 + k^2} \tag{7}$$

Both (k) and (R) are related to the refractive index (n) according to Fresnel's Eq. 7 [31]. The values of n as calculated from Eq. 6 are plotted in Fig. 5 as a function of the wavelength (λ) and for all Dy_2O_3 concentrations. The refractive index exhibits a noticeable and gradual increase with increasing Dy_2O_3 content. Such increase in the values of n is consistent with the observed increase in the density and the average coordination number of the glass network, where both factors lead to the increase of NBO.

$$\alpha h\upsilon = A_o\left(h\upsilon - E_g^{opt}\right)^n \tag{8}$$

In order to investigate the optical induced electronic transitions in the studied samples, the Mott and Davis Eq. 8 could be used to calculate the optical energy gap (E_g^{opt}) [32, 33]. In this equation, $n = 2$, 3, 1/2, or 1/3, which corresponds to indirect allowed, indirect forbidden, direct allowed and direct forbidden transitions, respectively. (A_o) is a parameter called the band tailing. The optical indirect band gap can be evaluated by plotting the quantity $(\alpha h\nu)^{0.5}$ versus the photon energy ($h\nu$) as shown in Fig. 6. The intercept of the best fit line of the band edge determines the optical band gap. On the other hand, the calculated tailing energy can be estimated via the determination of Urbach's energy E_u from Eq. 9 [33],

$$\alpha = \alpha_0 \exp\left(\frac{h\nu}{E_U}\right) \tag{9}$$

By applying the least square fitting technique on the plot of the ln (α) versus hν in the localized states (see Fig. 7), the value of (E_u) can be calculated. The dependence of optical band gap and Urbach's energy on the Dy_2O_3 content are plotted in Fig. 8. It observed that (E_g^{opt}) decreased, while (E_u) increased with increasing Dy_2O_3 content. Such large reduction (> 1 eV) of the optical band gap can be attributed to the increase in the number of NBOs, which is strongly related to the absorption of sample. The growth of non-bridging oxygen results

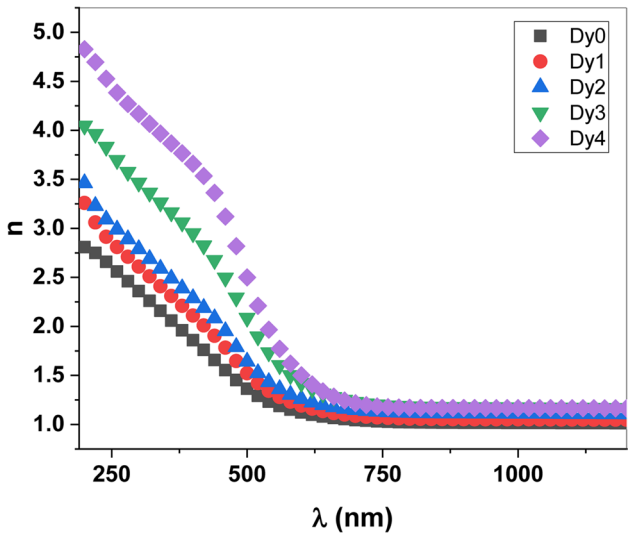

Fig. 5 Composition and wavelength dependence of n for the studied glasses

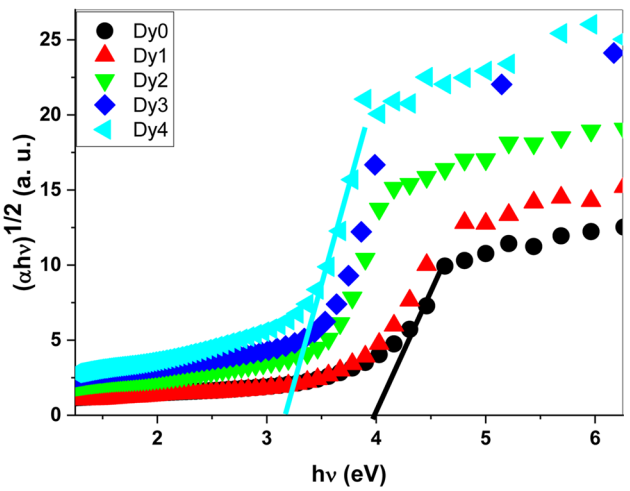

Fig. 6 The energy dependence of the absorption coefficient parameters $(\alpha h\nu)^{0.5}$ for the studied glass samples

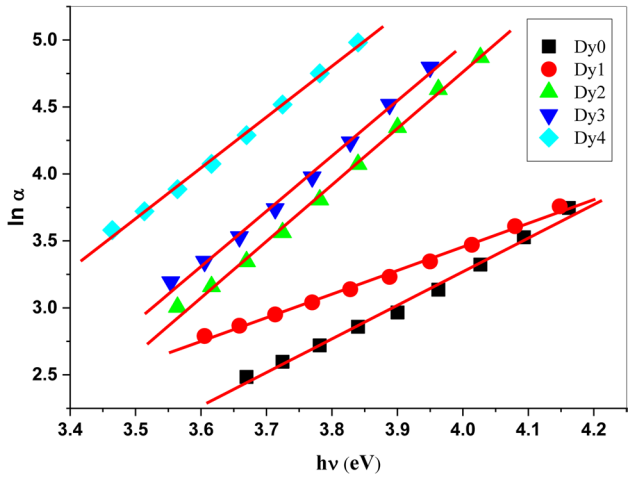

Fig. 7 ln(α) versus hν, for the studied glass samples

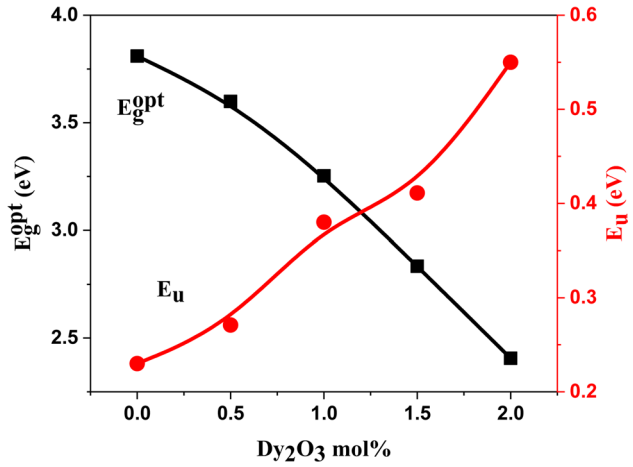

Fig. 8 The variation of both E_g^{opt} and E_u as function of Dy_2O_3 content

from the conversion of BO_4 to BO_3 units (indicated from FTIR results) [34, 35]. However, the increase in the values of (E_u) reflects increasing randomness of the glass matrix with Dy_2O_3 [36–42].

Electric conductivity

The AC conductivity measured total conductivity [σ_t (ω, T)] for all samples must follow Eq. 10, where σ_{ac} and σ_{dc} are the ac and dc conductivity, respectively, *A* is a weakly temperature dependent factor, *s* is the exponent factor, and ω is the angular frequency [43, 44].

$$\sigma_t = \sigma_{ac} + \sigma_{dc} \tag{10a}$$

$$\sigma_t = A\omega^s + \sigma_{dc} \tag{10b}$$

The total conductivity of all investigated glasses is measured over the temperature range extending from 300 to 675 K at different frequencies 120 Hz, 1 kHz, 10 kHz, and 100 kHz. The temperature dependence of total conductivity (σ_t) for the sample Dy_0 as a representative sample is depicted in Fig. 9 at lower temperatures (300–440 K); σ_t exhibits weak temperature-dependence and strong frequency dispersion for all samples. However, at temperatures above 440, the total conductivity shows a frequency-independent behavior and rapid boost with increasing temperature. Therefore, it can be stated that the dc conductivity is dominant at high temperatures, while the ac conductivity dominates at low temperatures. It is also concluded that all our samples behave like semiconductors [43].

Fig. 10 presents the relationship between ln (σ_t) and 1000/T in the temperature range (540-640K) at fixed frequency (10^5 Hz) for all samples. The linear behavior of this relation for all samples indicates that the total conductivity of all investigated glasses is thermally activated in this working temperature range and follows the Arrhenius Eq. 11 [39, 45], where $\sigma_0$the pre-exponential factor and *K* is Boltzmann constant.

$$\sigma_{dc} = \sigma_0 \, e^{-\frac{\Delta E_g}{kT}} \tag{11}$$

According to the Arrhenius equation, the electron activation energies (ΔE_g) can be estimated by taking the slopes of the best fit lines of the ln (σ_t)-1000/T plots. Fig. 12 displays the variation of both ln (σ_t) and (ΔE_g) with Dy_2O_3 content. It is noted that ln (σ_t) decreases, while (ΔE_g) increases by the replacement of B_2O_3 by Dy_2O_3. The reduction of the conductivity can be attributed to the decrease in Na^+ ions mobility due to the blocking effect of Dy^{3+} cations in the glass

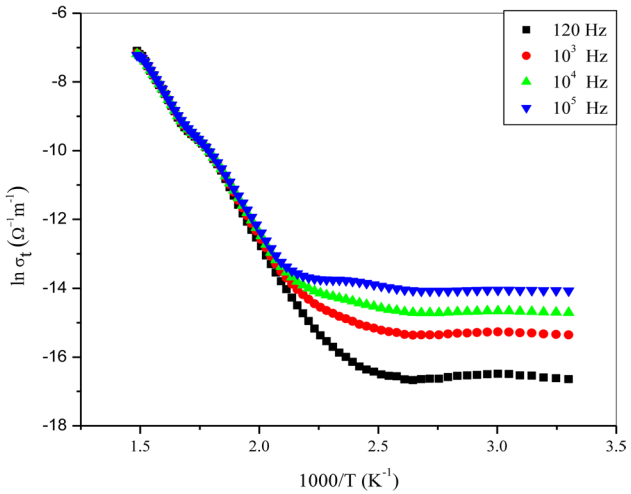

Fig. 9 The temperature dependence total conductivity for the sample Dy_0 at four different frequencies as a representative example

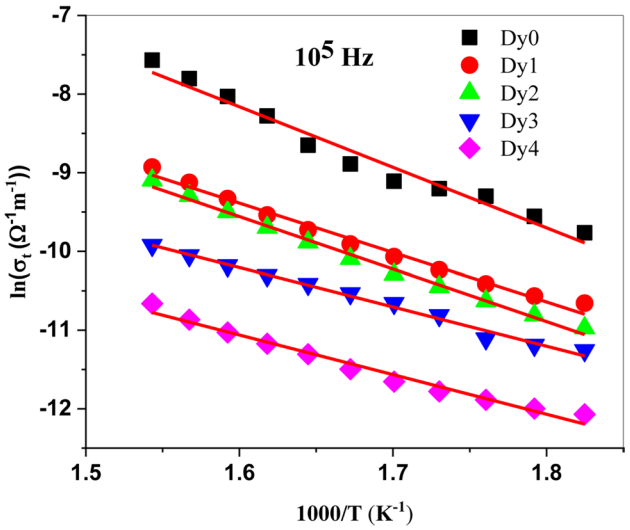

Fig. 10 Total conductivity temperature dependence for all the studied glasses up to 570 K and at 10^5 Hz

network. From Fig. 11, it could also be inferred that (ΔE_g) exhibits practically the reverse behavior of the conductivity [46], a trend which is logically expected. The values of the exponent factors (s) can also be calculated using Eq. 12:

$$s = \frac{\ln\left(\sigma_t\right)}{\ln(\omega)} \tag{12}$$

The obtained values of (s) are plotted, in Fig. 12, as a function of temperature for the Dy_2 sample as a representative example since all samples show similar behaviors. The obtained values of (s) for all samples suggest two conduction mechanisms. The first is taking place in the range 300–450 K, where (s) increased with increasing temperature, indicating that the dominant conduction mechanism is the

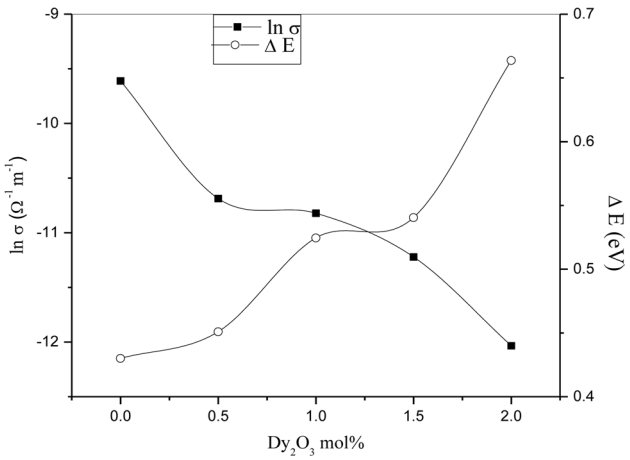

Fig. 11 The variation of both ln σ_t and ΔE_g with Dy_2O_3 concentration

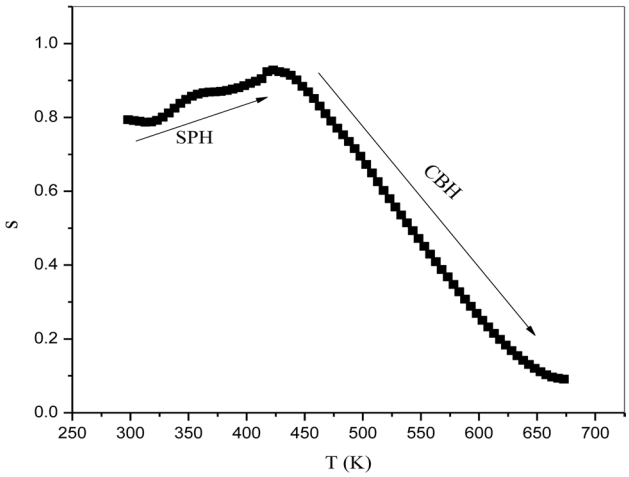

Fig. 12 The change in s-factor as a function of temperature for the sample G_3 as a representative curve

small polaron hopping (SPH), model. The second mechanism occurs at a higher temperature in the range 450–675 K, where (s) show a gradual decrease in temperature. This behavior appears to be consistent with the experimental behavior of (s) for the correlated barrier hopping (CBH) mechanism [47]. Therefore, it is assumed that the CBH model can describe the conduction mechanism in such a range of temperatures.

Dielectric relaxation

The temperature dependence of the dielectric constant (ε') for sample Dy_0, as a representative example, is seen in Fig. 13 at four different frequencies (120, 10^3, 10^4, and 10^5 Hz). It can be

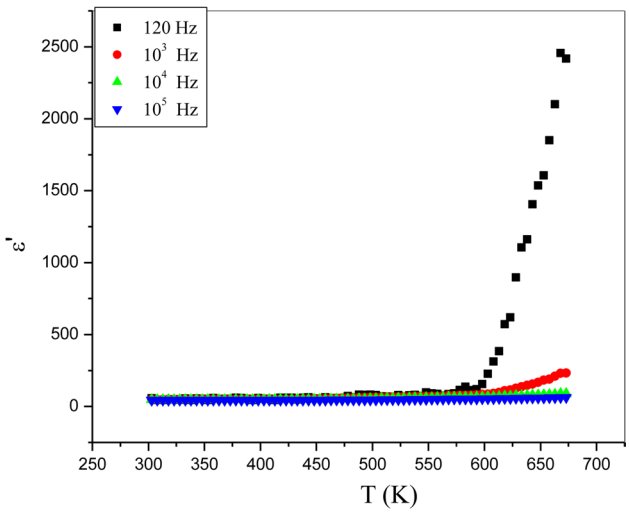

Fig. 13 The dielectric constant (ε') temperature dependent at four frequencies for the sample Dy_0 as a representative curve

noticed that at lower temperatures (below 500 K), the dielectric constant is independent on temperature; however, it decreases with increasing frequency at relatively higher temperatures. This behavior can be attributed to the reduction of dipolar polarization and interfacial polarization [48]. At higher frequencies, the charge carriers do not have enough time to follow the electric field reversal. The dipolar polarization results from the orientation of permanent dipoles in the electric field direction. In contrast, interfacial polarization can be attributed to the impedance of the charge carrier's movement at the interfaces [49]. Such impedance could be due to the thermal vibration of the molecules affecting the orientational polarization [50] and/or to the space charge polarization originated from bond defects within the network structure [51]. Fig. 14 shows the dielectric loss factor (ε'') temperature dependence for the sample G_1 measured at four different frequencies (120, 10^3, 10^4, and 10^5 Hz). It is clear that ε'' increases with increasing the temperature, and the same behavior is obtained for all samples. It was stated by Mott et al. [52] that, when the sample is placed between the electrodes, the hopping of electron will occur between the localized sites in such a way that charge carriers move through the sites, hopping from donors to acceptors. Consequently, every pair of these sites produces a dipole. In this respect, the dielectric properties of glasses can be explained by recognizing such a set of dipoles. Every dipole has its own relaxation time which relies on its activation energy [53]. This is due to the presence of a potential barrier (W_m) that each carrier will hop through [54]. Such a potential barrier originates from the Coulomb interaction between neighboring sites of the dipole. Guintini et al. [55] suggested that the loss factor ε'' in glass materials at a certain frequency within the studied temperature range must obey the power law in the following Eq. 13, where B is a constant. Therefore, the relation between ln (ε'') and ln (ω) for the glass Dy_0 is plotted at various temperatures in Fig. 15.

$$\varepsilon'' = B\,\omega^m \tag{13}$$

The values of m can be estimated from slopes of the above mentioned relation and are associated with the potential barrier (W_m) by Eq. 14:

$$m = \frac{-4\pi kT}{W_m} \tag{14}$$

Consequently, the values of (W_m) can be calculated and listed in Table 3. It is found that these calculated values of potential barrier are well agree with the hopping charge carriers method over a barrier proposed by Elliott [54] for amorphous materials. The variations of (ε') and (ε'') with the gradual increase of Dy_2O_3 at fixed frequency of 10^4 Hz and constant temperature of 573 K are listed in Table 3. Both quantities decrease with increasing Dy_2O_3 content, likely due to both dipolar and interfacial polarization. This is also due to the dielectric polarization process and the dc conduction [56].

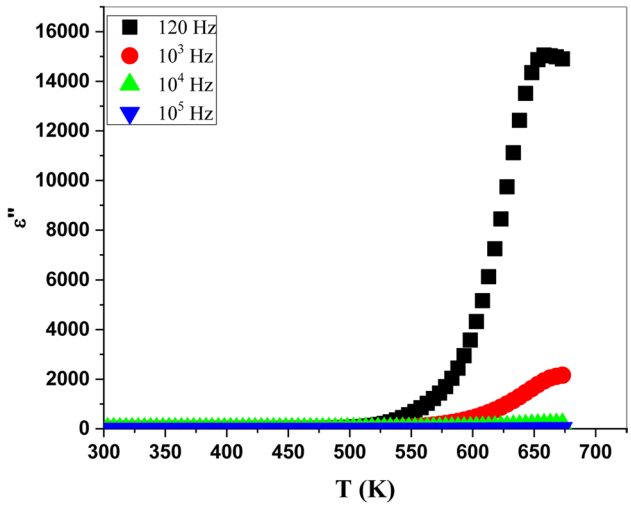

Fig. 14 The dielectric loss (ε') temperature dependent at four different frequencies for the sample Dy_0 as representative curve

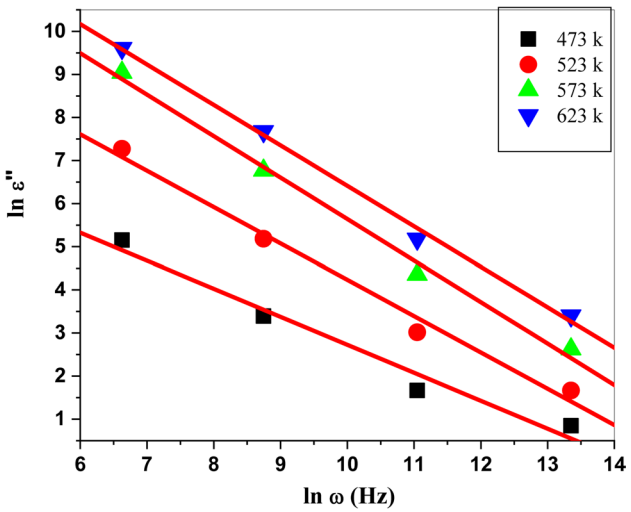

Fig. 15 The dielectric loss (ε'') as a function of frequency at different temperatures for Dy_0, as a representative curve

Table 3 Real ε' and imaginary ε'' dielectric constant, the potential barrier W_m, and the activation energy ΔE_D

Sample	ε'	ε''	W_m (eV)	ΔE_D (eV)
Dy_0	56.269	102.27	0.129	0.458
Dy_1	52.55	77.36	0.135	0.499
Dy_2	47.23	57.90	0.138	0.531
Dy_3	43.72	17.86	0.141	0.587
Dy_4	40.95	14.22	0.151	0.678

Electric modulus

The real and imaginary parts of the electric modulus (M') and (M'') give information on the mechanism of the ionic conductivity in the lack of a clear dielectric loss peak [57]. Therefore, (M') and (M'') will be calculated by using Eqs. 15 and 16.

$$M' = \frac{\varepsilon'}{\left(\varepsilon^{\varepsilon 2} + \varepsilon'^{2}\right)} \tag{15}$$

$$M^{\varepsilon} = \frac{\varepsilon^{\varepsilon}}{\left(\varepsilon^{\varepsilon 2} + \varepsilon'^{2}\right)} \tag{16}$$

Fig. 16 shows the temperature dependence of the real parts of the electric modulus at different frequencies for the glass Dy_0 as a representative sample. It is observed that M' attains minimal values approaching zero at lower frequencies due to the lack of an electrode polarization effect [58]. As the frequency increases, M' increases noticeably, which can be attributed to the distribution of relaxation processes at limited range of frequencies [59]. The region between the low and high-frequency elevation defines the frequency range in which these ions can move. Within these domains, the corresponding well-defined peak in (M'') spectra is shown in Fig. 17. Such observed peaks can rarely be shown for all the studied glasses, and they reflect the movement of the charge carriers responsible for the dc conductivity. This behavior may occur due to the superposition of various relaxation processes related to the NBO formation and different structural variations. The imaginary modulus (M'') will be used to calculate the dipole activation energy of the dielectric using Eq. 17 since the maximum peak height is not available to obtain from the temperature dependence of tan (δ),

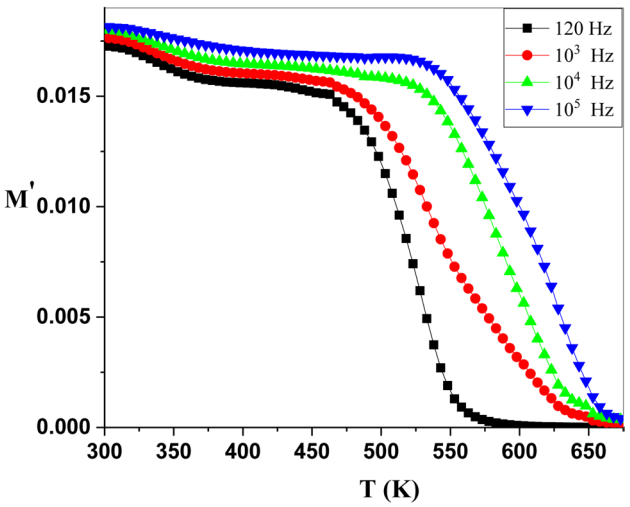

Fig. 16 The real dielectric modulus as a function of both frequency and temperature for sample Dy_0, as a representative curve

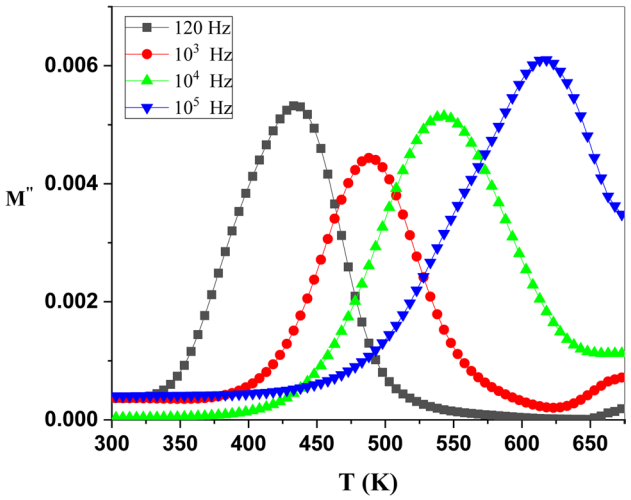

Fig. 17 The real and imaginary dielectric modulus as a function of both frequency and temperature for sample Dy_0, as a representative curve

where ($\tau = 1/f$) is the relaxation time and (ΔE_D) the activation energy of dipoles of a dielectric [60].

$$\tau = \tau_o \exp\left(\frac{\Delta E_D}{kT}\right) \tag{17}$$

Fig. 17 illustrates the variation of M'' with the temperature at four different frequencies (120, 10^3, 10^4, and 10^5 Hz). It is observed that all the studied samples feature a clear relaxation peak at a certain temperature (T_m), which is shifting toward a higher temperature as the frequency was increased. This behavior characterizes the relaxation of the dielectric loss in the studied samples, which may be associated with the orientation polarization frequency. By the aid of Fig. 18, the value of the temperature at maximum (T_m) for each corresponding frequency can be extracted. Therefore, the activation energy for conductivity relaxation time can be calculated by plotting the relation between ln(τ) and $1000/T_m$, depicted in Fig. 18. Table 3 gives the change of (ΔE_D) as a function of Dy_2O_3 content. It is found that the activation energy increase with increasing Dy_2O_3 concentration. This result can be associated with the lower value of conductivity which supports the resistive nature of doped sample [61].

Radiation shielding study

Phy-X program has been applied to conduct theoretical calculations of several of shielding factors [62], choosing energies that ranged from 0.284 to 1.33 MeV. These energies are representative of the typical energies produced by Co-60, Cs-137, and Na-22 sources that are employed in an extensive number of various uses in the real world. We attempted to comprehend

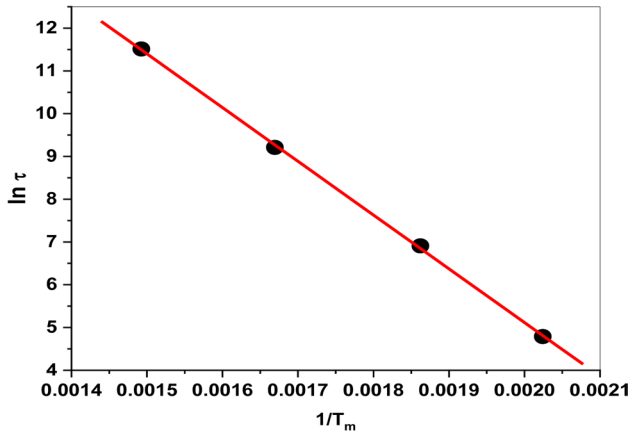

Fig. 18 ln (τ) and $1000/T_m$

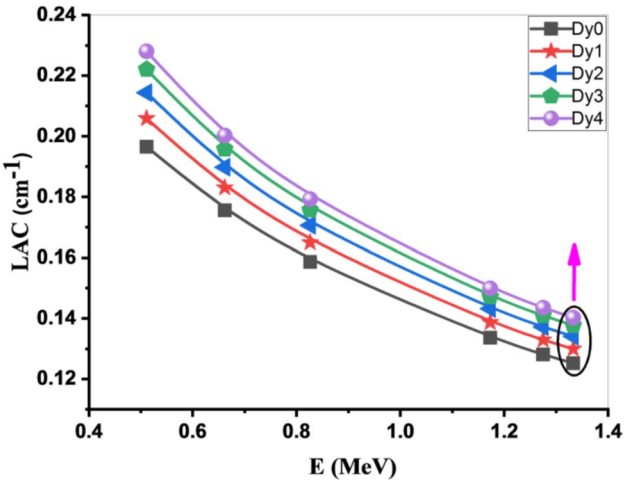

Fig. 19 The linear attenuation coefficient of our prepared Dy_0–Dy_4 glasses

how the chemical composition impacts the radiation shielding factors by varying the amount of Dy_2O_3 and Al_2O_3 in the glasses, giving us an understanding of the effect of these variables on the overall shielding behavior. In order to fully comprehend the glasses' possible uses, we also attempted to assess the shielding effectiveness of the glasses across a range of energy levels, including low- and high-energy radiation. In addition, we investigated the effect that the density of the glasses had on the radiation-blocking capabilities of the glasses; this has allowed us to gain a deeper comprehension of the variables that influence the radiation-blocking capabilities of glasses. As a first step toward comprehending the radiation shielding ability of the Dy0–Dy4 glasses that we had produced, we looked into the linear attenuation coefficient, also known by its abbreviation LAC.

Fig. 19 shows the change in the LAC as a function of energy for our glasses. The behavior of the LAC as a function of energy is comparable to the LAC patterns that were obtained for various other glass systems in the published research [63], confirming the accuracy of the Phy-X results. From **Fig. 19**, we noticed that the LAC has an inverse relationship with energy by observing that the highest LAC occurred at the first chosen energy (around 0.248–0.32 cm^{-1}), and the minimum LAC occurred at the last chosen energy (0.125–0.140 cm^{-1}). This would imply that the glasses act as efficient attenuators when subjected to low-energy radiation; however, their effectiveness would go down with increasing energy, and they would be least efficient at the highest energy. In addition, we found that the LAC differs for various glass formulations, which is evidence that it is dependent on the glass's constituents. In particular, we observed an increase in the LAC as the amount of Dy_2O_3 increased from 0 to 2.5 mol%; this is consistent with the increase in the density of the glasses. As the density of the glasses increases, a greater number of photons are able to interact with the atoms, which results in an increase in photon absorption and scattering, which leads to an increase in the number of photons that are attenuated within the sample.

The effective atomic number (Z_{eff}) represents one of the parameters that may be employed for further study of the radiation shielding characteristics of the glasses that have been prepared. This characteristic is especially helpful when working with shielding materials that consist of a variety of elements or compounds [64]. We are able to use Z_{eff} to comprehend how the inclusion of Dy_2O_3 affects the Z_{eff} of our glasses because these glasses contain fixed quantities of Na_2O and Al_2O_3, as well as different quantities of B_2O_3 and Dy_2O_3. In addition, we are able to acquire a more in-depth comprehension of the shielding characteristics of the glasses when subjected to various radiation energies if we investigate the change in Z_{eff} when subjected to different energy values.

Fig. 20 presents the Z_{eff} values for the Dy_0–Dy_4 glasses. It is clear from the findings that the incorporation of Dy_2O_3 into the glasses has a substantial effect on the Z_{eff}. The value of the Z_{eff} for the Dy0 sample, which does not include any Dy_2O_3 (that is, the concentration of Dy_2O_3 is equal to zero), stays relatively the same, ranging around 7.51. This is because the Dy_0 sample is composed of up of the elements B, O, Na, and Al, all of which have atomic numbers that are relatively close to one another, which results in a nearly uniform Z_{eff}. However, as we continued to add Dy_2O_3 to the glasses, we noticed that the Z_{eff} altered with energy, particularly at low energies. This led us to conclude that Dy_2O_3 has an effect on the Z_{eff} of the samples. Even though the increase in Dy_2O_3 content is only very slight (0.5 mol% in each stage), it has an effect on the Z_{eff}, and our findings show that the Z_{eff} gets higher as we progress from Dy_1 to Dy_4.

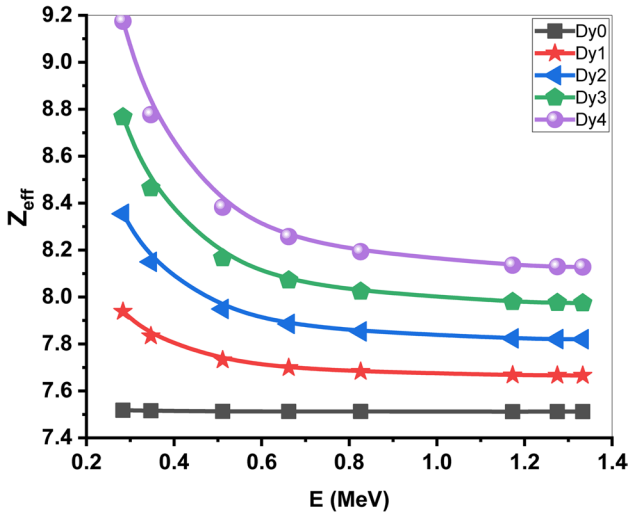

Fig. 20 The effective atomic number of our prepared Dy_0–Dy_4 glasses

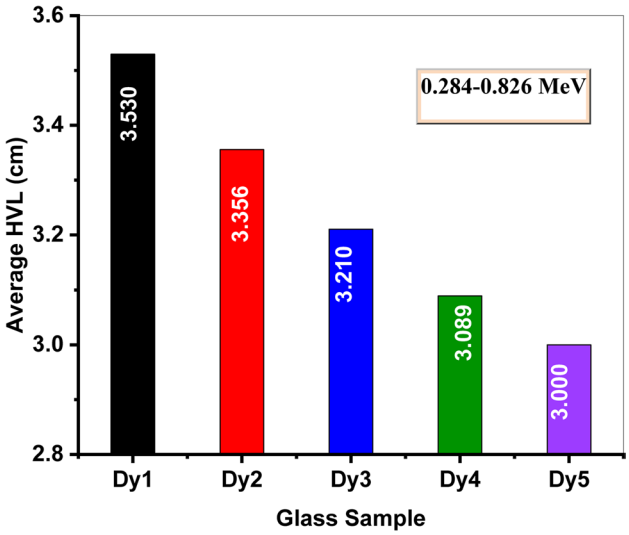

Fig. 21 The average half value layer $\left(\overline{HVL}\right)$ for the Dy_0–Dy_4 glasses for E less than 0.826 MeV

For Dy_1 to Dy_4 glasses, we noticed two different regions in the of Z_{eff} figure. The first region corresponds to energies between 0.284 and 0.826 MeV, whereas the second region is associated with energies that are higher than 0.826 MeV. When compared to the second region, we found that the rate of reduction in Z_{eff} was significantly greater in the first region. This is because the photoelectric effect is more prevalent in the first region, whereas the Compton scattering is more prevalent in the second region. Therefore, for low energies, the Z_{eff} of the glasses is very reliant on the energy, whereas at higher energies, it is just slightly reliant on the energy. The fact that Dy_4 showed the highest Z_{eff} among the prepared glasses indicates that Dy_2O_3 is a useful high-Z compound that increases the radiation shielding characteristics of glasses. This conclusion was reached as a result of the observation that Dy_4 displayed the highest Z_{eff} among the prepared glasses. This conclusion was reached as a result of the finding that Dy_4 exhibited the highest Z_{eff} among the prepared glasses. Due to the high atomic number of dysprosium, which makes it more effective in the attenuation of radiation than materials with a lower Z value, the value of Z_{eff} increases when the concentration of Dy_2O_3 increases as well. As a consequence of this, the addition of Dy_2O_3 to the glasses improves both their capacity to absorb and their capability to scatter ionizing radiation.

It is of the greatest significance to determine the actual thickness of the material that must be used in order to block a given amount of incoming photons. It is vital to investigate the idea of the half-value layer in order to calculate the thickness that must be present in order to block out fifty percent of the photon intensity [65]. The HVL is affected by a number of parameters, notably the energy of the beam of photons, the composition and density of the shielding material. As a result, it is absolutely necessary to do research into the effect that these parts have on the HVL of our samples. We have computed the average half value layer ($\overline{HVL}$) for two distinct energy zones, one for E that is lower than 0.826 MeV and the other for E that is higher than 0.826 MeV. Both of these regions have been considered separately. We are able to determine the necessary thickness of glass for real-world applications by using this (HVL) value, which is based on the particular radiation that would be present. If we want to employ the glasses for purposes that involve low-energy radiation, we must utilize the (HVL) value that has been determined for region 1. Conversely, we should produce glasses with a thickness comparable to the result for region 2 if we need to use them for high-energy radiation activities.

Figures 21 and 22 show that results of the $\overline{HVL}$ in (i.e., for region 1 and region 2, respectively). The data showed that the $\overline{HVL}$is higher in the second region than the first zone, with numerical values span from 5.38 to 4.79 cm in region 2 and 3.53–3.00 cm for region 1. According to these data, if the energy if the photons is smaller than 0.826 MeV, then we need a glass with a small thickness in order to provide suitable protection. But, greater thickness must be used if the energy of the radiation higher than 0.826 MeV. Moreover, the data given in both figures demonstrated that the $\overline{HVL}$ depends on the amount of Dy_2O_3 in the glasses. In a brief, we observed that the $\overline{HVL}$ decreases with inclusion Dy_2O_3 in the glasses. This reduction in the $\overline{HVL}$ is correct at both energy range (i.e., in Figs. 22 and 23). As a result, our results imply that adding Dy_2O_3 to glasses may result in better radiation attenuation qualities, especially in situations involving lower radiation energy.

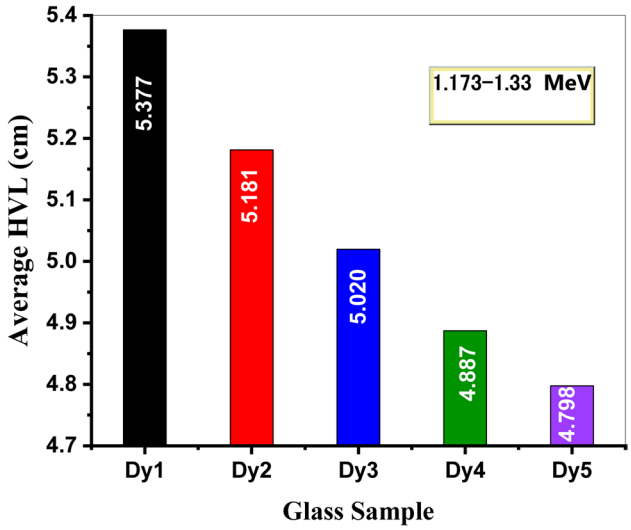

Fig. 22 The average half value layer$\left(\overline{HVL}\right)$ for the Dy_0–Dy_4 glasses for E greater than 0.826 MeV

The mean free path (MFP) is a crucial element in measuring the effectiveness of a shielding material in reducing radiation dosage and plays a crucial role in selecting the best compounds for specific radiation types and intensities. In order to correctly forecast how radiation will behave inside a material, optimize the shield's thickness and composition, and improve the safety and efficiency of radiation-dependent processes and applications, it is critical to have a thorough understanding of the MFP. We presented the MFP for the Dy_0–Dy_4 glasses in Fig. 24. The MFP of the Dy_0–Dy_4 glasses exhibited a considerable reliance on energy, with the MFP found to be at its lowest value at the 0.284 MeV energy level, which was the smallest energy level studied in the present investigation. The MFP values that were the lowest ranged anywhere from 4.026 cm for Dy_0 glasses to 3.129 cm for Dy_4 glass. For E=0.347 MeV, we observed an increase in the MFP and the MFP for Dy_0 increases to 4.35 cm and the MFP for Dy_4 is 3.56 cm. The MFP displays continuous growth as energy levels keep on increase, eventually achieving maximum values of 7.98 and 7.13 cm for Dy_0 and Dy_4, respectively, at the specified energy peak of 1.33 MeV. These results highlight how important it is to take into account the energy levels while coming up with effective methods for radiation shielding. According to the findings of this research, there is an obvious relationship between the amount of Dy_2O_3 present in glasses and the MFP. For example, the MFP reduces from 4.03 cm for Dy0 to 3.13 cm for Dy4 when the energy is 0.284 MeV, which corresponds to a reduction of around 22%. In a similar way the MFP decreases from 4.35 cm for Dy_0 to 3.56 cm for Dy_4, which corresponds to a decrease of about 18%. At higher energies, the impact remains evident but significantly less pronounced. Numerically, at 0.511 MeV, the MFP reduces from 5.09 cm for Dy_0 glass to 4.39 cm for Dy_4 sample, which is a reduction of 13.8%, while at 1.33 MeV, the MFP values changed between 7.99 and 7.13 cm for Dy_0 and Dy_4 which is a decrease of about 10.7%. These numerical results provide further evidence that higher levels of Dy_2O_3 lead to the Dy_0–Dy_4 glasses' possessing radiation attenuation capabilities that are superior in effectiveness. It seems that the influence is more noticeable at lower energy levels, lending credence to the notion that the incorporation of Dy_2O_3 has an especially significant impact on the glass's capacity to absorb radiation with a low-energy radiation.

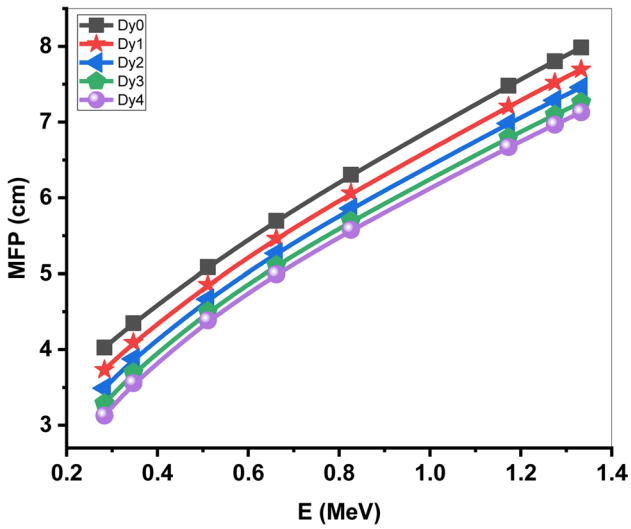

Fig. 23 The mean free path (MFP) for the Dy_0–Dy_4 glasses

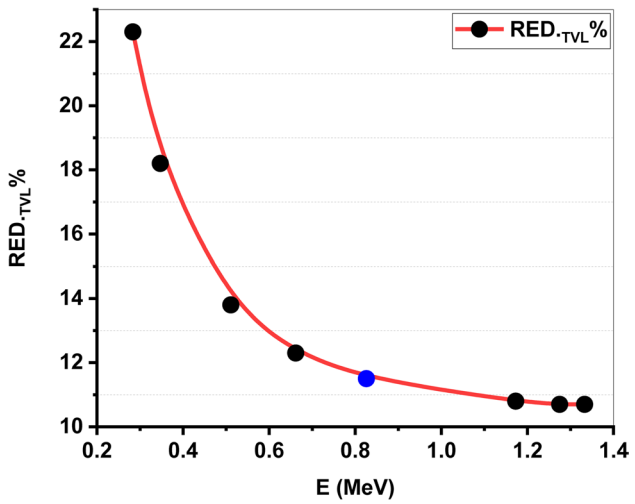

Fig. 24 The reduction in the TVL ($RED._{TVL}$) for the glasses Dy_0–Dy_4 due to the addition of Dy_2O_3

The tenth value layer (TVL) has been estimated and then determined the reduction in the TVL ($RED._{TVL}$) for the Dy0–Dy4 samples due to the inclusion of Dy_2O_3. In the ($RED._{TVL}$), we compared the TVL for the samples with lowest and highest amount of Dy_2O_3 (i.e., Dy_0 and Dy_4) and plotted the results in Fig. 24. The reduction in TVL for each energy level shows how much the introduction of Dy_2O_3 has enhanced the samples' radiation shielding abilities. With a TVL drop of 22.3% at 0.284 MeV, the impact is more noticeable at lower energies and less so as it increases. This could be caused by the photoelectric effect, which is more pronounced at lower energy. $RED._{TVL}$ values between 12.3 and 10.7% for energies between 0.662 and 1.33 MeV indicate a nearly continuous decline in TVL as energy levels increase. This implies that the shielding performance remains stable at higher energy region. The noticed pattern might be relied on by the Compton scattering effect becoming more dominant at higher energy. The Compton scattering effect is less dependent on the atomic number of the elements contained in the shielding substance than is the photoelectric effect. This characteristic may be the cause of the more regular fall in TVL observed at high energy values.

Conclusion

Five sodium aluminoborate glasses doped with Dy^{3+} ions were prepared using the conventional melt quenching technique. Their structures as well as the optical and electrical properties were thoroughly investigated. According to these studies, the following conclusions were drawn. The density was found to increase, while the molar volume was found to decrease with Dy_2O_3 increasing. The changes in the FTIR spectra for the studied samples can be attributed to the transformation of BO_4 to BO_3 structural units. The Urbach energy was shown to increase and the optical band gap is decreased indicating an increase of NBO with Dy_2O_3 additives. The electrical conductivity exhibits a decreasing trend as Dy^{3+} ions were increased. This is due to Dy^{3+} ions block the mobility of Na^+ ions. The SPH and CHB models are the predominant conduction mechanisms at low and high temperatures, respectively. Using Phy-X software, we reported the radiation shielding factors for the prepared glasses, and we examined the impact of Dy_2O_3 on the attenuation performance of these glasses. Both LAC and Z_{eff} quantities demonstrated that the inclusion of Dy_2O_3 into the current glasses causes an improvement in the attenuation capabilities of the glasses. The $\overline{HVL}$ when the E<0.826 is higher than that for E>0.826 MeV. Also, the $\overline{HVL}$ depends on the amount of Dy_2O_3 in the glasses. The $\overline{HVL}$ data also proved that the inclusion of Dy_2O_3 in the glasses causes a reduction the HVL, which means an improvement in the attenuation performance of these glasses will happen if we use more amount of Dy_2O_3.

Funding Open access funding provided by The Science, Technology & Innovation Funding Authority (STDF) in cooperation with The Egyptian Knowledge Bank (EKB).

Data availability All data will be available at required.

Declarations

Conflict of interest The authors declare no competing interests.

References

1. İlhan, M., Ekmekçi, M.K.: Synthesis and photoluminescence properties of Dy3+ doped white light emitting CdTa2O6 phosphors. J. Solid State Chem. **226**, 243 (2015)
2. Ramteke, D., Gedam, R.: Spectroscopic properties of dysprosium oxide containing lithium borate glasses. Spectrosc. Lett. **48**, 417 (2015)
3. Gaafar, M., Marzouk, S.: Mechanical and structural studies on sodium borosilicate glasses doped with Er2O3 using ultrasonic velocity and FTIR spectroscopy. Phys. B Condens. Matter. **388**, 294 (2007)
4. Babu, Y.C.R., Naik, P.S.R., Kumar, K.V., Kumar, N.R., Kumar, A.S.: Spectral investigations of Sm3+ doped lead bismuth magnesium borophosphate glasses. J. Quant. Spectrosc. Radiat. Transf. **113**, 1669 (2012)
5. Selvi, S., Venkataiah, G., Arunkumar, S., Muralidharan, G., Marimuthu, K.: Structural and luminescence studies on Dy3+ doped lead boro–telluro-phosphate glasses. Phys. B Condens. Matter. **454**, 72 (2014)
6. Reduan, S., Hashim, S., Ibrahim, Z., Alajerami, Y., Mhareb, M., Maqableh, M., Dawaud, R., Tamchek, N.: Physical and optical properties of Li2O–MgO–B2O3 doped with Sm3+. J. Mol. Struct. **1060**, 6 (2014)
7. Pawar, P., Munishwar, S., Gedam, R.: Physical and optical properties of Dy3+/Pr3+ Co-doped lithium borate glasses for W-LED. J. Alloys Compd. **660**, 347 (2016)
8. Mhareb, M., Hashim, S., Ghoshal, S., Alajerami, Y., Bqoor, M., Hamdan, A., Saleh, M., Karim, M.A.: Effect of Dy2O3 impurities on the physical, optical and thermoluminescence properties of lithium borate glass. J. Lumin. **177**, 366 (2016)
9. Pawar, P., Munishwar, S., Gautam, S., Gedam, R.: Physical, thermal, structural and optical properties of Dy3+ doped lithium alumino-borate glasses for bright W-LED. J. Lumin. **183**, 79 (2017)
10. Ibrahim, A.M.: Fabrication and characterization of CeO2-doped glasses and nano-glass–ceramics for UV protection sunglasses. Appl. Phys. A **127**, 947 (2021). https://doi.org/10.1007/s00339-021-05093-5

11. Minakova, N.A., Zaichuk, A.V., Belyi, Y.I.: The structure of borate glass. Glas. Ceram. **65**, 70 (2008)
12. Anishia, S.R., Jose, M.T., Annalakshmi, O., Ponnusamy, V., Ramasamy, V.: Dosimetric properties of rare earth doped LiCaBO3 thermoluminescence phosphors. J. Lumin. **130**, 1834 (2010)
13. Monisha, M., D'souza, A.N., Hegde, V., Prabhu, N.S., Sayyed, M., Lakshminarayana, G., Kamath, S.D.: Dy3+ doped SiO2–B2O3–Al2O3–NaF–ZnF2 glasses: an exploration of optical and gamma radiation shielding features. Curr. Appl. Phys. **20**, 1207 (2020)
14. Mahani, R.M., Marzouk, S.Y.: AC conductivity and dielectric properties of SiO2–Na2O–B2O3–Gd2O3 glasses. J. Alloys Compd. **579**, 394 (2013)
15. Abrahams, I., Hadzifejzovic, E.: Lithium ion conductivity and thermal behaviour of glasses and crystallised glasses in the system Li2O–Al2O3–TiO2–P2O5. Solid State Ionics. **134**, 249 (2000)
16. Abdel-Baki, M., Salem, A., Abdel-Wahab, F., El-Diasty, F.: Bond character, optical properties and ionic conductivity of Li2O/B2O3/SiO2/Al2O3 glass: Effect of structural substitution of Li2O for LiCl. J. Non-Cryst. Solids. **354**, 4527 (2008)
17. Kaky, K.M., Lakshminarayana, G., Baki, S., Taufiq-Yap, Y., Kityk, I., Mahdi, M.: Structural, thermal, and optical analysis of zinc boro-aluminosilicate glasses containing different alkali and alkaline modifier ions. J. Non-Cryst. Solids. **456**, 55 (2017)
18. Wong, P.S., Wan, M.H., Hussin, R., Lintang, H.O., Endud, S.: Structural and luminescence studies of europium ions in lithium aluminium borophosphate glasses. J. Rare Earths. **32**, 585 (2014)
19. Arunkumar, S., Venkataiah, G., Marimuthu, K.: Spectroscopic and energy transfer behavior of Dy3+ ions in B2O3TeO2PbOPbF2Bi2O3CdO glasses for laser and WLED applications. Spectrochim. Acta A Mol. Biomol. Spectrosc. **136**, 1684 (2015)
20. Kıbrıslı, O., Ersundu, A., Ersundu, M.Ç.: Dy3+ doped tellurite glasses for solid-state lighting: an investigation through physical, thermal, structural and optical spectroscopy studies. J. Non-Cryst. Solids. **513**, 125 (2019)
21. Arunkumar, S., Krishnaiah, K.V., Marimuthu, K.: Structural and luminescence behavior of lead fluoroborate glasses containing Eu3+ ions. Phys. B Condens. Matter. **416**, 88 (2013)
22. Pascuta, P., Borodi, G., Culea, E.: Influence of europium ions on structure and crystallization properties of bismuth borate glasses and glass ceramics. J. Non-Cryst. Solids. **354**, 5475 (2008)
23. Mansour, E.: Semi-quantitative analysis for FTIR spectra of Al2O3-PbO-B2O3-SiO2 glasses. J. Non-Cryst. Solids. **358**, 454 (2012)
24. Kaur, P., Kaur, S., Singh, G.P., Singh, D.: Cerium and samarium codoped lithium aluminoborate glasses for white light emitting devices. J. Alloys Compd. **588**, 394 (2014)
25. Tarte, P.: Infra-red spectra of inorganic aluminates and characteristic vibrational frequencies of AlO4 tetrahedra and AlO6 octahedra. Spectrochim. Acta A: Mol. Spectrosc. **23**, 2127 (1967)
26. Kaur, P., Singh, G.P., Kaur, S., Singh, D.: Modifier role of cerium in lithium aluminium borate glasses. J. Mol. Struct. **1020**, 83 (2012)
27. Nanda, K., Kundu, R.S., Punia, R., Mohan, D., Kishore, N.: Resonant and non-resonant nonlinear optical properties of Er3+ modified BaO-ZnO-B2O3 glasses at 532 and 1550 nm. J. Non-Cryst. Solids. **541**, 120155 (2020)
28. Wang, Z., Zhao, Z., Peng, B., Liu, D., Xu, H., Chen, Y., Wang, D., Liu, H., Peng, N.: Investigation on the mechanism of the immobilization of CeO2 by using cullet-based glass (CBG). Ann. Nucl. Energy. **133**, 209 (2019)
29. Juan, L., Zhang, C., Qiang, T., Jingquan, H., Zhang, Y., Qiang, S., Shubin, W.: Photoluminescence and thermoluminescence properties of dysprosium doped zinc metaborate phosphors. J. Rare Earths. **26**, 203 (2008)
30. Elbashar, Y.H., Ali, M.I., Elshaikh, H.A., A.G.: El-Din Mostafa, Influence of CuO and Al2O3 addition on the optical properties of sodium zinc phosphate glass absorption filters. Optik. **127**, 7041 (2016)
31. Saddeek, Y.B., Aly, K., Abbady, G., Afify, N., Shaaban, K.S., Dahshan, A.: Optical and structural evaluation of bismuth alumina-borate glasses doped with different amounts of (Y2O3). J. Non-Cryst. Solids. **454**, 13 (2016)
32. Davis, E.A., Mott, N.: Electronic processes in non-crystalline materials. Clarendon Press, Oxford (1971)
33. Shaaban, E.R., Hassaan, M.Y., Moustafa, M., Qasem, A., Ali, G.A.: Optical constants, dispersion parameters and non-linearity of different thickness of As40S45Se15 thin films for optoelectronic applications. Optik. **186**, 275 (2019)
34. Sadeq, M.S., Abdo, M.A.: Effect of iron oxide on the structural and optical properties of alumino-borate glasses. Ceramics International **47**, 2043–2049 (2021)
35. Moustafa, M.G., Shreif, A., Ghalab, S.: Towards superior optical and dielectric properties of borosilicate glasses containing tungsten and vanadium ions. Mater. Chem. Phys. **254**, 123464 (2020)
36. Berkemeier, F., Voss, S., Imre, Á.W., Mehrer, H.: Molar volume, glass-transition temperature, and ionic conductivity of Na-and Rb-borate glasses in comparison with mixed Na–Rb borate glasses. J. Non-Cryst. Solids. **351**, 3816 (2005)
37. Urbach, F.: The long-wavelength edge of photographic sensitivity and of the electronic absorption of solids. Phys. Rev. **92**, 1324 (1953)
38. Abdel-Baki, M., Abdel-Wahab, F., Radi, A., El-Diasty, F.: Factors affecting optical dispersion in borate glass systems. J. Phys. Chem. Solids. **68**, 1457 (2007)
39. Reddy, R., Ahammed, Y.N., Azeem, P.A., Gopal, K.R., Rao, T.: Electronic polarizability and optical basicity properties of oxide glasses through average electronegativity. J. Non-Cryst. Solids. **286**, 169 (2001)
40. Umar, S.A., Halimah, M.K., Chan, K.T., Latif, A.A.: Polarizability, optical basicity and electric susceptibility of Er3+ doped silicate borotellurite glasses. J. Non-Cryst. Solids. **471**, 101 (2017)
41. Duffy, J., Ingram, M.D.: An interpretation of glass chemistry in terms of the optical basicity concept. J. Non-Cryst. Solids. **21**, 373 (1976)
42. Bhatia, B., Meena, S., Parihar, V., Poonia, M.: Optical basicity and polarizability of Nd 3+-doped bismuth borate glasses. New J. Glass Ceram. **5**, 44 (2015)
43. Abdel-Ghany, A., Bendary, A., Abou-El-Nasr, T., Hassaan, M., Mostafa, A.: Electrical transport properties of some sodium silicate glasses containing by-pass cement dust. Nat. Sci. **12**, 6 (2014)
44. El-Desoky, M.M., Hassaan, M.Y., El-Kottamy, M.: WO 3 concentration and frequency dependence of conductivity and dielectric constant of sodium borate tungstate glasses. J. Mater. Sci. Mater. Electron. **9**, 447 (1998)
45. Elliott, S.: Temperature dependence of ac conductivity of chalcogenide glasses. Philos. Mag. B. **37**, 553 (1978)
46. El-Desoky, M., Ibrahim, F., Mostafa, A., Hassaan, M.: Effect of nanocrystallization on the electrical conductivity enhancement and Mössbauer hyperfine parameters of iron based glasses. Mater. Res. Bull. **45**, 1122 (2010)
47. Elliott, S.: A theory of ac conduction in chalcogenide glasses. Philos. Mag. **36**, 1291 (1977)
48. Ibrahim, A.M.: Impact of MoO3 concentration, frequency and temperature on the dielectric properties of zinc phosphate glasses. ChJPh. **68**, 919 (2020)
49. Ibrahim, A.M., Elbashar, Y.H., Badr, A.M., Elshaikh, H.A., Mostafa, A.G.: Mixed ionic–polaronic conduction in copper sodium phosphate glasses containing aluminium oxide. J. Microw. Power Electromagn. Energy. **51**, 71 (2017)

50. Yakuphanoglu, F.: Electrical conductivity and electrical modulus properties of α, ω-dihexylsexithiophene organic semiconductor. Phys. B Condens. Matter. **393**, 139 (2007)
51. Schütt, H.: A new phenomenological description of the electrical relaxation in ionic conductors. Solid State Ionics. **72**, 86 (1994)
52. Mott, N., Davis, E., Street, R.: States in the gap and recombination in amorphous semiconductors. Philos. Mag. **32**, 961 (1975)
53. Shakra, A., Farid, A., Hegab, N., Afifi, M., Alrebati, A.: Conduction mechanism and dielectric properties of a Se 80 Ge 20− x Cd x (x= 0, 6 and 12 at. wt%) films. Appl. Phys. A Mater. Sci. Process. **122**, 1 (2016)
54. Elliott, S.: Ac conduction in amorphous chalcogenide and pnictide semiconductors. Adv. Phys. **36**, 135 (1987)
55. Giuntini, J., Zanchetta, J., Jullien, D., Eholie, R., Houenou, P.: Temperature dependence of dielectric losses in chalcogenide glasses. J. Non-Cryst. Solids. **45**, 57 (1981)
56. James, A., Prakash, C., Prasad, G.: Structural properties and impedance spectroscopy of excimer laser ablated Zr substituted BaTiO3 thin films. J. Phys. D. Appl. Phys. **39**, 1635 (2006)
57. Hazra, S., Ghosh, A.: ac relaxation mechanism in some cuprate glasses. Phys. Rev. B. **55**, 6278 (1997)
58. Patro, L.N., Hariharan, K.: AC conductivity and scaling studies of polycrystalline SnF2. Mater. Chem. Phys. **116**, 81 (2009)
59. Langar, A., Sdiri, N., Elhouichet, H., Ferid, M.: Conductivity and dielectric behavior of NaPO3–ZnO–V2O5 glasses. J. Alloys Compd. **590**, 380 (2014)
60. Mostafa, A., Abdel-Wahab, F., Yahya, G.: Dielectric relaxation and ac conductivity of titanium-substituted iron in boron-based glasses. J. Mater. Sci. Mater. Electron. **13**, 721 (2002)
61. Rayssi, C., Kossi, S., Dhahri, J., Khirouni, K.: Frequency and temperature-dependence of dielectric permittivity and electric modulus studies of the solid solution Ca0.85Er0.1Ti1−xCo4x/3O3 (0 ≤ x ≤ 0.1). RSC Adv. **8**, 17139 (2018)
62. Şakar, E., Özpolat, Ö.F., Bünyamin Alım, M.I., Sayyed, M.K.: Phy-X / PSD: Development of a user friendly online software for calculation of parameters relevant to radiation shielding and dosimetry. Radiat. Phys. Chem. **166**, 108496 (2020)
63. Acikgoz, A., Demircan, G., Yılmaz, D., Aktas, B., Yalcin, S., Yorulmaz, N.: Structural, mechanical, radiation shielding properties and albedo parameters of alumina borate glasses: Role of CeO2 and Er2O3. Mater. Sci. Eng. B. **276**, 115519 (2022). https://doi.org/10.1016/j.mseb.2021.115519
64. Kamislioglu, M.: An investigation into gamma radiation shielding parameters of the (Al:Si) and (Al+Na):Si-doped international simple glasses (ISG) used in nuclear waste management, deploying Phy-X/PSD and SRIM software. J. Mater. Sci. Mater. Electron. **32**, 12690–12704 (2021)
65. Kamislioglu, M.: Research on the effects of bismuth borate glass system on nuclear radiation shielding parameters. Result in Phys. **22**, 103844 (2021)